

1000+ FPS 4D Gaussian Splatting for Dynamic Scene Rendering

Yuan Yuheng Qihong Shen Xingyi Yang Xinchao Wang
National University of Singapore

{yuhengyuan, qihong.shen, xyang}@u.nus.edu, xinchao@nus.edu.sg



Figure 1. **Compressibility and Rendering Speed.** We introduce **4DGS-1K**, a novel compact representation with high rendering speed. In contrast to 4D Gaussian Splatting (4DGS) [40], we can achieve rasterization at 1000+ FPS while maintaining comparable photorealistic quality with only 2% of the original storage size. The right figure is the result tested on the N3V [18] datasets, where the radius of the dot corresponds to the storage size.

Abstract

4D Gaussian Splatting (4DGS) has recently gained considerable attention as a method for reconstructing dynamic scenes. Despite achieving superior quality, 4DGS typically requires substantial storage and suffers from slow rendering speed. In this work, we delve into these issues and identify two key sources of temporal redundancy. (Q1) **Short-Lifespan Gaussians:** 4DGS uses a large portion of Gaussians with short temporal span to represent scene dynamics, leading to an excessive number of Gaussians. (Q2) **Inactive Gaussians:** When rendering, only a small subset of Gaussians contributes to each frame. Despite this, all Gaussians are processed during rasterization, resulting in redundant computation overhead. To address these redundancies, we present **4DGS-1K**, which runs at over 1000 FPS on modern GPUs. For Q1, we introduce the *Spatial-Temporal Variation Score*, a new pruning criterion that effectively removes short-lifespan Gaussians while encouraging 4DGS to capture scene dynamics using Gaussians with longer temporal spans. For Q2, we store a mask for active Gaussians across consecutive frames, significantly reducing redundant computations in rendering. Compared to vanilla 4DGS, our method achieves a $41\times$ reduction in storage and $9\times$ faster rasterization speed on complex dynamic scenes, while maintaining comparable visual quality. Please see our project page at [4DGS-1K](#).

1. Introduction

Novel view synthesis for dynamic scenes allows for the creation of realistic representations of 4D environments, which is essential in fields like computer vision, virtual reality, and augmented reality. Traditionally, this area has been led by neural radiance fields (NeRF) [2, 12, 18, 21, 25], which model opacity and color over time to depict dynamic scenes. While effective, these NeRF-based methods come with high training and rendering costs, limiting their practicality, especially in real-time applications and on devices with limited resources.

Recently, point-based representations like 4D Gaussian Splatting (4DGS) [40] have emerged as strong alternatives. 4DGS models a dynamic scene using a set of 4D Gaussian primitives, each with a 4-dimensional mean and a 4×4 covariance matrix. At any given timestamp, a 4D Gaussian is decomposed into a set of conditional 3D Gaussians and a marginal 1D Gaussian, the latter controlling the opacity at that moment. This mechanism allows 4DGS to effectively capture both static and dynamic features of a scene, enabling high-fidelity dynamic scene reconstruction.

However, representing dynamic scenes with 4DGS is both storage-intensive and slow. Specifically, 4DGS often requires millions of Gaussians, leading to significant storage demands (averaging 2GB for each scene on the N3V [18] dataset) and suboptimal rendering speed. In com-

parison, mainstream deformation field methods [39] require only about 90MB for the same dataset. Therefore, reducing the storage size of 4DGS [40] and improving rendering speed are essential for efficiently representing complex dynamic scenes.

We look into the cause of such an explosive number of Gaussian and place a specific emphasis on two key issues. **(Q1)** A large portion of Gaussians exhibit a short temporal span. In empirical experiments, 4DGS tends to favor “flicking” Gaussians to fit complex dynamic scenes, which just influence a short portion of the temporal domain. This necessitates that 4DGS relies on a large number of Gaussians to reconstruct a high-fidelity scene. As a result, substantial storage is needed to record the attributes of these Gaussians: **(Q2)** Inactive Gaussians lead to redundant computation. During rendering, 4DGS needs to process all Gaussians. However, only a very small portion of Gaussians are active at that moment. Therefore, most of the computation time is spent on inactive Gaussians. This phenomenon greatly hampers the rendering speed. In this paper, we introduce **4DGS-1K**, a framework that significantly reduces the number of Gaussians to minimize storage requirements and speedup rendering while maintaining high-quality reconstruction. To address these issues, 4DGS-1K introduces a two-step pruning approach:

- **Pruning Short-Lifespan Gaussians.** We propose a novel pruning criterion called the *spatial-temporal variation score*, which evaluates the temporal impact of each Gaussian. Gaussians with minimal influence are identified and pruned, resulting in a more compact scene representation with fewer Gaussians with short temporal span.
- **Filtering Inactive Gaussians.** To further reduce redundant computations during rendering, we use a key-frame temporal filter that selects the Gaussians needed for each frame. On top of this, we share the masks for adjacent frames. This is based on our observation that Gaussians active in adjacent frames often overlap significantly.

Besides, the pruning in step 1 enhances the masking process in step 2. By pruning Gaussians, we increase the temporal influence of each Gaussian, which allows us to select sparser key frames and further reduce storage requirements.

We have extensively tested our proposed model on various dynamic scene datasets including real and synthetic scenes. As shown in Fig. 1, 4DGS-1K reduces storage costs by $41\times$ on the Neural 3D Video datasets [18] while maintaining equivalent scene representation quality. Crucially, it enables real-time rasterization speeds exceeding 1,000 FPS. These advancements collectively position 4DGS-1K as a practical solution for high-fidelity dynamic scene modeling without compromising efficiency.

In summary, our contributions are three-fold:

- We delve into the temporal redundancy of 4D Gaussian Splatting, and explain the main reason for the storage

pressure and suboptimal rendering speed.

- We introduce **4DGS-1K**, a compact and memory-efficient framework to address these issues. It consists of two key components, a spatial-temporal variation score-based pruning strategy and a temporal filter.
- Extensive experiments demonstrate that 4DGS-1K not only achieves a substantial storage reduction of approximately $41\times$ but also accelerates rasterization to 1000+ FPS while maintaining high-quality reconstruction.

2. Related Work

2.1. Novel view synthesis for static scenes

Recently, neural radiance fields(NeRF) [25] have achieved encouraging results in novel view synthesis. NeRF [25] represents the scene by mapping 3D coordinates and view dependency to color and opacity. Since NeRF [25] requires sampling each ray by querying the MLP for hundreds of points, this significantly limits the training and rendering speed. Subsequent studies [5, 11, 26, 31, 32, 35, 37, 38] have attempted to speed up the rendering by introducing specialized designs. However, these designs also constrain the widespread application of these models. In contrast, 3D Gaussian Splatting(3DGS) [14] has gained significant attention, which utilizes anisotropic 3D Gaussians to represent scenes. It achieves high-quality results with intricate details, while maintaining real-time rendering performance.

2.2. Novel view synthesis for dynamic scenes

Dynamic NVS poses new challenges due to the temporal variations in the input images. Previous NeRF-based dynamic scene representation methods [2, 4, 12, 17, 18, 21, 24, 30, 34, 36] handle dynamic scenes by learning a mapping from spatiotemporal coordinates to color and density. Unfortunately, these NeRF-based models are constrained in their applications due to low rendering speeds. Recently, 3D Gaussians Splatting [14] has emerged as a novel explicit representation, with many studies [3, 6, 13, 22, 39, 41] attempting to model the dynamic scenes based on it. 4D Gaussian Splatting(4DGS) [40] is one of the representatives. It utilizes a set of 4D Gaussian primitives. However, 4DGS often requires a huge redundant number of Gaussians for dynamic scenes. These Gaussians lead to tremendous storage and suboptimal rendering speed. To this end, we focus on analyzing the temporal redundancy of 4DGS [40] in hopes of developing a novel framework to achieve lower storage requirements and higher rendering speeds.

2.3. Gaussian Splatting Compression

3D Gaussian-based large-scale scene reconstruction typically requires millions of Gaussians, resulting in the requirement of up to several gigabytes of storage. Therefore, subsequent studies have attempted to tackle these is-

sues. Specifically, Compgs [27] and Compact3D [16] employ vector quantization to store Gaussians within codebooks. Concurrently, inspired by model pruning, some studies [1, 8, 9, 20, 28, 29] have proposed criterion to prune Gaussians by a specified ratio. However, compared to 3DGS [14], 4DGS [40] introduces an extra temporal dimension to enable dynamic representation. Previous 3DGS-based methods may therefore be unsuitable for 4DGS. Consequently, we first identify a key limitation leading to this problem, referred as *temporal redundancy*. Furthermore, we propose a novel pruning criterion leveraging spatial-temporal variation, and a temporal filter to achieve more efficient storage requirements and higher rendering speed.

3. Preliminary of 4D Gaussian Splatting

Our framework builds on 4D Gaussian Splatting (4DGS) [40], which reconstructs dynamic scenes by optimizing a collection of *anisotropic 4D Gaussian primitives*. For each Gaussian, it is characterized by a 4D mean $\mu = (\mu_x, \mu_y, \mu_z, \mu_t) \in \mathbb{R}^4$ coupled with a covariance matrix $\Sigma \in \mathbb{R}^{4 \times 4}$.

By treating time and space dimensions equally, the 4D covariance matrix Σ can be decomposed into a scaling matrix $S_{4D} = (s_x, s_y, s_z, s_t) \in \mathbb{R}^4$ and a rotation matrix $R_{4D} \in \mathbb{R}^{4 \times 4}$. R_{4D} is represented by a pair of left quaternion $q_l \in \mathbb{R}^4$ and right quaternion $q_r \in \mathbb{R}^4$.

During rendering, each 4D Gaussian is decomposed into a conditional 3D Gaussian and a 1D Gaussian at a specific time t . Moreover, the conditional 3D Gaussian can be derived from the properties of the multivariate Gaussian with:

$$\begin{aligned} \mu_{xyz|t} &= \mu_{1:3} + \Sigma_{1:3,4} \Sigma_{4,4}^{-1} (t - \mu_t) \\ \Sigma_{xyz|t} &= \Sigma_{1:3,1:3} - \Sigma_{1:3,4} \Sigma_{4,4}^{-1} \Sigma_{4,1:3} \end{aligned} \quad (1)$$

Here, $\mu_{1:3} \in \mathbb{R}^3$ and $\Sigma_{1:3,1:3} \in \mathbb{R}^{3 \times 3}$ denote the spatial mean and covariance, while μ_t and $\Sigma_{4,4}$ are scalars representing the temporal components. To perform rasterization, given a pixel under view \mathcal{I} and timestamp t , its color $\mathcal{I}(u, v, t)$ can be computed by blending visible Gaussians that are sorted by their depth:

$$\mathcal{I}(u, v, t) = \sum_i^N c_i(d) \alpha_i \prod_{j=1}^{i-1} (1 - \alpha_j) \quad (2)$$

with

$$\begin{aligned} \alpha_i &= p_i(t) p_t(u, v|t) \sigma_i \\ p_i(t) &\sim \mathcal{N}(t; \mu_t, \Sigma_{4,4}) \end{aligned} \quad (3)$$

where $c_i(d)$ is the color of each Gaussian, and α_i is given by evaluating a 2D Gaussian with covariance Σ_{2D} multiplied with a learned per-point opacity σ_i and temporal Gaussian distribution $p_i(t)$. In the following discussion, we denote $\Sigma_{4,4}$ as Σ_t for simplicity.

Temporal Redundancy. Despite achieving high quality, 4DGS requires a huge number of Gaussians to model dynamic scenes. We identify a key limitation leading to this problem: 4DGS represents scenes through temporally independent Gaussians that lack explicit correlation across time. This means that, even static objects are redundantly represented by hundreds of Gaussians, which inconsistently appear or vanish across timesteps. We refer to this phenomenon as *temporal redundancy*. As a result, scenes end up needing more Gaussians than they should, leading to excessive storage demands and suboptimal rendering speeds. In Sec. 4, we analyze the root causes of this issue and propose a set of solutions to reduce the count of Gaussians.

4. Methodology

Our goal is to compress 4DGS by reducing the number of Gaussians while preserving rendering quality. To achieve this, we first analyze the redundancies present in 4DGS, as detailed in Sec. 4.1. Building on this analysis, we introduce 4DGS-1K in Sec. 4.2, which incorporates a set of compression techniques designed for 4DGS. 4DGS-1K enables rendering speeds of over 1,000 FPS on modern GPUs.

4.1. Understanding Redundancy in 4DGS

This section investigates why 4DGS requires an excessive number of Gaussians to represent dynamic scenes. In particular, we identify two key factors. First, 4DGS models object motion using a large number of transient Gaussians that inconsistently appear and disappear across timesteps, leading to redundant temporal representations. Second, for each frame, only a small fraction of Gaussians actually contribute to the rendering. We discuss those problems below.

Massive Short-Lifespan Gaussians. We observe that 4DGS tends to store numerous Gaussians that flicker in time. We refer to these as *Short-Lifespan Gaussians*. To investigate this property, we analyze the Gaussians’ opacity, which controls visibility. Intuitively, Short-Lifespan Gaussians exhibit an opacity pattern that rapidly increases and then suddenly decreases. In 4DGS, this behavior is typically reflected in the time variance parameter Σ_t —small Σ_t values indicate a short lifespan.

Observations. Specifically, we plot the distribution of Σ_t for all Gaussians in the *Sear Steak* scene. As shown in Fig. 2a, most of Gaussians has small Σ_t values (e.g. 70% have $\Sigma_t < 0.25$). Moreover, as shown in Fig. 3, we visualize the spatial distribution of Σ_t values. We take the reciprocal of Σ_t and then normalize it. Therefore, brighter regions in the image indicate smaller Σ_t . Most of these Gaussians are concentrated along the edges of moving objects.

Therefore, in 4DGS, nearly all Gaussians have a short lifespan, especially around the fast-moving objects. This property leads to high storage needs and slower rendering.

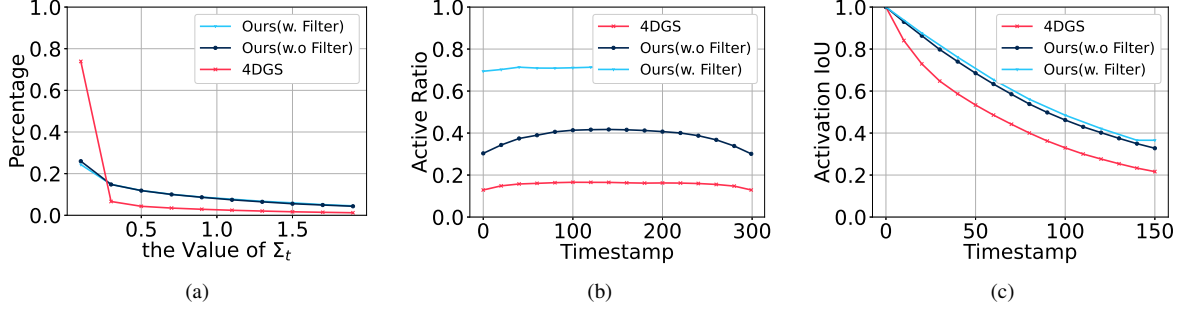


Figure 2. **Temporal redundancy Study.** (a) The Σ_t distribution of 4DGS. The red line shows the result of vanilla 4DGS. The other two lines represent our model has effectively reduced the number of transient Gaussians with small Σ_t . (b) The active ratio during rendering at different timestamps. It demonstrates that most of the computation time is spent on inactive Gaussians in vanilla 4DGS. However, 4DGS-1K can significantly reduce the occurrence of inactive Gaussians during rendering to avoid unnecessary computations. (c) This figure shows the IoU between the set of active Gaussians in the first frame and frame t . It proves that active Gaussians tend to overlap significantly across adjacent frames.

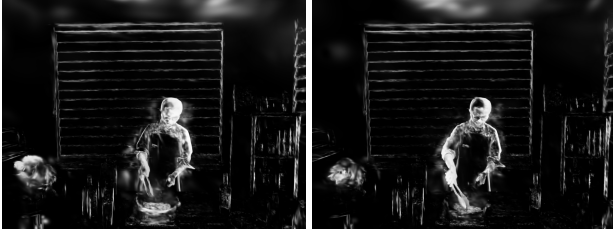


Figure 3. **Visualizations of Distribution of Σ_t .** Most of these Gaussians are concentrated along the edges of moving objects.

Inactive Gaussians. Another finding is that, during the forward rendering, actually, only a small fraction of Gaussians are contributing. Interestingly, active ones tend to overlap significantly across adjacent frames. To quantify this, we introduce two metrics: (1) *Active ratio*. This ratio is defined as the proportion of the total number of active Gaussians across all views at any moment relative to the total number of Gaussians. (2) *Activation Intersection-over-Union (IoU)*. This is computed as IoU between the set of active Gaussians in the first frame and in frame t .

Observations. Again, we plot the two metrics from *Sear Steak* scene. As shown in Fig. 2b, nearly 85% of Gaussians are inactive at each frame, even though all Gaussians are processed during rendering. Moreover, Fig. 2c demonstrates that the active Gaussians remain quite consistent over time, with an IoU above 80% over a 20-frame window.

The inactive gaussians bring a significant issue in 4DGS, because each 4D Gaussian must be decomposed into a 3D Gaussian and a 1D Gaussian before rasterization (see Eq. (1)). Therefore, a large portion of computational resources is wasted on inactive Gaussians.

In summary, redundancy in 4DGS comes from massive Short-Lifespan Gaussians and inactive Gaussians. These insights motivate our compression strategy to eliminate re-

dundant computations while preserving rendering quality.

4.2. 4DGS-1K for Fast Dynamic Scene Rendering

Building on the analysis above, we introduce 4DGS-1K, a suite of compression techniques specifically designed for 4DGS to eliminate redundant Gaussians. As shown in Fig. 4, this process involves two key steps. First, we identify and globally prune unimportant Gaussians with low Spatial-Temporal Variation Score in Sec. 4.2.1. Second, we apply local pruning using a temporal filter to inactive Gaussians that are not needed at each timestep in Sec. 4.2.2.

4.2.1. Pruning with Spatial-Temporal Variation Score

We first prune unimportant 4D Gaussians to improve efficiency. Like 3DGS, we remove those that have a low impact on rendered pixels. Besides, we additionally remove short-lifespan Gaussians—those that persist only briefly over time. To achieve this, we introduce a novel spatial-temporal variation score as the pruning criterion for 4DGS. It is composed of two parts, *spatial score* that measures the Gaussians contributions to the pixels in rendering, and *temporal score* considering the lifespan of Gaussians.

Spatial score. Inspired by the previous method [8, 9] and α -blending in 3DGS [14], we define the spatial score by aggregating the ray contribution of Gaussian g_i along all rays r across all input images at a given timestamp. It can accurately capture the contribution of each Gaussian to one pixel. Consequently, the spatial contribution score \mathcal{S}^S is obtained by traversing all pixels:

$$\mathcal{S}_i^S = \sum_{k=1}^{NHW} \alpha_i \prod_{j=1}^{i-1} (1 - \alpha_j) \quad (4)$$

where $\alpha_i \prod_{j=1}^{i-1} (1 - \alpha_j)$ reflects the contribution of i^{th} Gaussian to the final color of all pixels according to the alpha composition in Eq. (2).

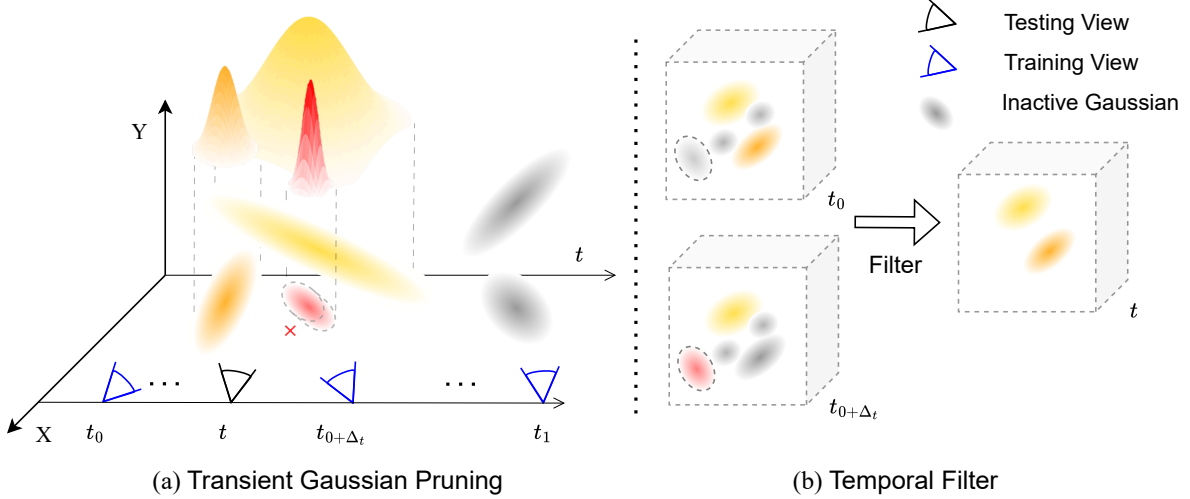


Figure 4. **Overview of 4DGS-1K.** (a) We first calculate the spatial-temporal variation score for each 4D Gaussian on training views, to prune Gaussians with short lifespan (The Red Gaussian). (b) The temporal filter is introduced to filter out inactive Gaussians before the rendering process to alleviate suboptimal rendering speed. At a given timestamp t , the set of Gaussians participating in rendering is derived from the two adjacent key-frames, t_0 and $t_{0+\Delta_t}$.

Temporal score. It is expected to assign a higher temporal score to Gaussians with a longer lifespan. To quantify this, we compute the *second derivative of* temporal opacity function $p_i(t)$ defined in Eq. (3). The second derivative $p_i^{(2)}(t)$ is computed as

$$p_i^{(2)}(t) = \left(\frac{(t - \mu_t)^2}{\Sigma_t^2} - \frac{1}{\Sigma_t} \right) p_i(t) \quad (5)$$

Intuitively, large second derivative magnitude corresponds to unstable, short-lived Gaussians, while low second derivative indicates smooth, persistent ones.

Moreover, since the second derivative spans the real number domain \mathbb{R} , we apply tanh function to map it to the interval $(0, 1)$. Consequently, the score for opacity variation, \mathcal{S}_i^{TV} , of each Gaussian $g_{i,t}$ is expressed as:

$$\mathcal{S}_i^{TV} = \sum_{t=0}^T \frac{1}{0.5 \cdot \tanh(|p_i^{(2)}(t)|) + 0.5}. \quad (6)$$

In addition to the opacity range rate, the volume of 4D Gaussians is necessary to be considered, as described in Eq. (1). The volume should be normalized following the method in [8], denoted as $\gamma(\mathcal{S}^{4D}) = \text{Norm}(V(\mathcal{S}^{4D}))$. Therefore, the final temporal score $\mathcal{S}_i^T = \mathcal{S}_i^{TV} \gamma(\mathcal{S}_i^{4D})$

Finally, by aggregating both spatial and temporal score, the spatial-temporal variation score \mathcal{S}_i can be written as:

$$\mathcal{S}_i = \sum_{t=0}^T \mathcal{S}_i^T \mathcal{S}_i^S \quad (7)$$

Pruning. All 4D Gaussians are ranked based on their spatial-temporal variation score \mathcal{S}_i , and Gaussians with

lower scores are pruned to reduce the storage burden of 4DGS [40]. The remaining Gaussians are optimized over a set number of iterations to compensate for minor losses resulting from pruning.

4.2.2. Fast rendering with temporal filtering

Our analysis reveals that inactive Gaussians induces unnecessary computations in 4DGS, significantly slowing down rendering. To address this issue, we introduce a temporal filter that dynamically selects active Gaussians. We observed that active Gaussians in adjacent frames overlap considerably (as detailed in Sec. 4.1), which allows us to share their corresponding masks across a window of frames.

Key-frame based Temporal Filtering. Based on this observation, we design a key-frame based temporal filtering for active Gaussians. We select sparse key-frames at even intervals and share their masks with surrounding frames.

Specifically, we select a list of key-frame timestamps $\{t_i\}_{i=0}^T$, where T depends on the chosen interval Δ_t . For each t_i , we render the images from all training views at current timestamp and calculate the visibility list $\{m_{i,j}\}_{j=1}^N$, where $m_{i,j}$ is the visibility mask obtained by Eq. (2) from the j^{th} training viewpoint at timestamp t_i and N is the number of training views at current timestamp. The final set of active Gaussian masks is given by $\left\{ \bigcup_{j=1}^N m_{i,j} \right\}_{i=0}^T$.

Filter based Rendering. To render the images from any viewpoint at a given timestamp t_{test} , we consider its two nearest key-frames, denoted as t_l and t_r . Then, we perform rasterization while only considering the Gaussians marked by mask $\left\{ \bigcup_{j=1}^N m_{i,j} \right\}_{i=l,r}$. This method explicitly filters

Table 1. Quantitative comparisons on the Neural 3D Video Dataset.

Method	PSNR \uparrow	SSIM \uparrow	LPIPS \downarrow	Storage(MB) \downarrow	FPS \uparrow	Raster FPS \uparrow	#Gauss \downarrow
Neural Volume ¹ [21]	22.80	-	0.295	-	-	-	-
DyNeRF ¹ [18]	29.58	-	0.083	28	0.015	-	-
StreamRF[17]	28.26	-	-	5310	10.90	-	-
HyperReel[2]	31.10	0.927	0.096	360	2.00	-	-
K-Planes[12]	31.63	-	0.018	311	0.30	-	-
Dynamic 3DGS[23]	30.67	0.930	0.099	2764	460	-	-
4DGaussian[39]	31.15	0.940	0.049	90	30	-	-
E-D3DGS[3]	31.31	0.945	0.037	35	74	-	-
STG[19]	32.05	0.946	0.044	200	140	-	-
4D-RotorGS[7]	31.62	0.940	0.140	-	277	-	-
MEGA[43]	31.49	-	0.056	25	77	-	-
Compact3D[16]	31.69	0.945	0.054	15	186	-	-
4DGS[40]	32.01	-	0.055	-	114	-	-
4DGS ² [40]	31.91	0.946	0.052	2085	90	118	3333160
Ours	31.88	0.946	0.052	418	805	1092	666632
Ours-PP	31.87	0.944	0.053	50	805	1092	666632

¹ The metrics of the model are tested without “coffee martini” and the resolution is set to 1024×768 .

² The retrained model from the official implementation.

Table 2. Quantitative comparisons on the D-NeRF Dataset.

Method	PSNR \uparrow	SSIM \uparrow	LPIPS \downarrow	Storage(MB) \downarrow	FPS \uparrow	Raster FPS \uparrow	#Gauss \downarrow
DNeRF[30]	29.67	0.95	0.08	-	0.1	-	-
TiNeuVox[10]	32.67	0.97	0.04	-	1.6	-	-
K-Planes[12]	31.07	0.97	0.02	-	1.2	-	-
4DGaussian[39]	32.99	0.97	0.05	18	104	-	-
Deformable3DGS[41]	40.43	0.99	0.01	27	70	-	131428
4D-RotorGS[7]	34.26	0.97	0.03	112	1257	-	-
4DGS[40]	34.09	0.98	0.02	-	-	-	-
4DGS ¹ [40]	32.99	0.97	0.03	278	376	1232	445076
Ours	33.34	0.97	0.03	42	1462	2482	66460
Ours-PP	33.37	0.97	0.03	7	1462	2482	66460

¹ The retrained model from the official implementation.

out inactive Gaussians to speed up rendering.

Note that using long intervals may overlook some Gaussians, reducing rendering quality. Therefore, we fine-tune Gaussians recorded by the masks to compensate for losses.

5. Experiment

5.1. Experimental Settings

Datasets. We utilize two dynamic scene datasets to demonstrate the effectiveness of our method: (1) **Neural 3D Video Dataset (N3V)** [18]. This dataset consists of six dynamic scenes, and the resolution is 2704×2028 . For a fair comparison, we align with previous work [19, 40] by conducting evaluations at a half-resolution of 300 frames. (2) **D-NeRF Dataset** [30]. This dataset is a monocular video dataset comprising eight videos of synthetic scenes. We choose standard test views that originate from novel camera positions not encountered during the training process.

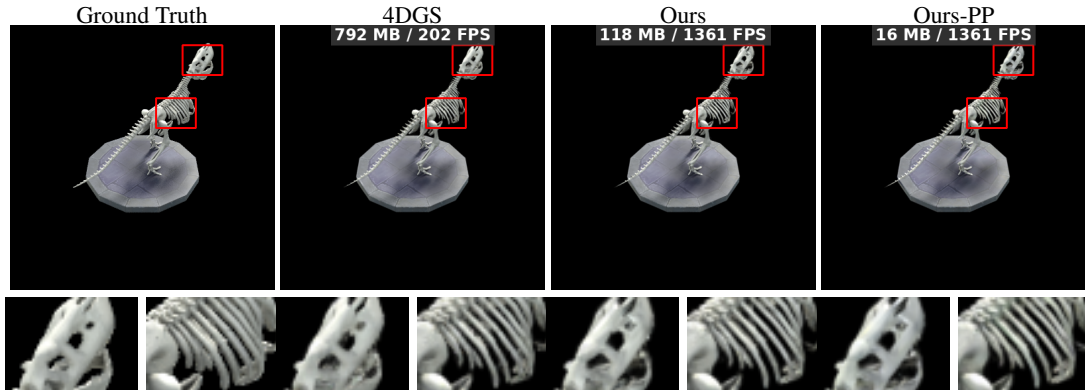
Evaluation Metrics. To evaluate the quality of rendering dynamic scenes, we employ several commonly used im-

age quality assessment metrics: Peak Signal-to-Noise Ratio (PSNR), Structural Similarity Index Measure (SSIM), and Learned Perceptual Image Patch Similarity (LPIPS) [42]. Following the previous work, LPIPS [42] is computed using AlexNet [15] and VGGNet [33] on the N3V dataset and the D-NeRF dataset, respectively. Moreover, we report the number of Gaussians and storage. To demonstrate the improvement in rendering speed, we report two types of FPS: (1) **FPS**. It considers the entire rendering function. Due to interference from other operations, it can’t effectively demonstrate the acceleration achieved by our method. (2) **Raster FPS**. It only considers the rasterization, the most computationally intensive component during rendering.

Baselines. Our primary baseline for comparison is 4DGS [40], which serves as the foundation of our model. Moreover, we compare 4DGS-1K with two concurrent works on 4D compression, MEGA [43] and Compact3D [16]. Certainly, we conduct comparisons with 4D-RotorGS [7] which is another form of representation for 4D Gaussian Splatting with the capability for real-time render-



(a) Results on Sear Steak Scene.



(b) Results on Trex Scene.

Figure 5. Qualitative comparisons of 4DGS and our method.

Table 3. Ablation study of per-component contribution.

ID	Method \ Dataset			PSNR \uparrow	SSIM \uparrow	LPIPS \downarrow	Storage(MB) \downarrow	FPS \uparrow	Raster FPS \uparrow	#Gauss \downarrow
	Filter	Pruning	PP							
a		vanilla 4DGS ¹		31.91	0.9458	0.0518	2085	90	118	3333160
b	\checkmark ^{1,2}			31.51	0.9446	0.0539	2091	242	561	3333160
c	\checkmark ²			29.56	0.9354	0.0605	2091	300	561	3333160
d			\checkmark	31.92	0.9462	0.0513	417	312	600	666632
e	\checkmark	\checkmark		31.88	0.9457	0.0524	418	805	1092	666632
f	\checkmark ²	\checkmark		31.63	0.9452	0.0524	418	789	1080	666632
g	\checkmark	\checkmark	\checkmark	31.87	0.9444	0.0532	50	805	1092	666632

¹ The result with environment map. ² The result without finetuning.

ing speed and high-fidelity rendering results. In addition, we also compare our work against NeRF-based methods, like Neural Volume [21], DyNeRF [18], StreamRF [17], HyperReel [2], DNeRF [30] and K-Planes [12]. Furthermore, other recent competitive Gaussian-based methods are also considered in our comparison, including Dynamic 3DGS [23], STG [19], 4DGAussian [39], and E-D3DGS [3].

Implementation Details. Our method is tested in a single RTX 3090 GPU. We train our model following the experiment setting in 4DGS [40]. After training, we perform the pruning and filtering strategy. Then, we fine-tune 4DGS-1K for 5,000 iterations while disabling additional clone/split

operations. For pruning strategy, the pruning ratio is set to 80% on the N3V Dataset, and 85% on the D-NeRF Dataset. For the temporal filtering, we set the interval Δ_t between key-frames to 20 frames on the N3V Dataset. Considering the varying capture speeds on the D-NeRF dataset, we select 6 key-frames rather than a specific frame interval. Additionally, to further compress the storage of 4DGS [40], we implement post-processing techniques in our model, denoted as Ours-PP. It includes vector quantization [27] on SH of Gaussians and compressing the mask of filter into bits.

Note that we don't apply environment maps implemented by 4DGS on Coffee Martini and Flame Salmon

scenes, which significantly affects the rendering speed. Subsequent results indicate that removing it for 4DGS-1K does not significantly degrade the rendering quality.

5.2. Results and Comparisons

Comparisons on real-world dataset. Tab. 1 presents a quantitative evaluation on the N3V dataset. 4DGS-1K achieves rendering quality comparable to the current baseline. Compared to 4DGS [40], we achieve a $41\times$ compression and $9\times$ faster in rendering speed at the cost of a $0.04dB$ reduction in PSNR. In addition, compared to MEGA [43] and Compact3D [16], two concurrent works on 4D compression, the rendering speeds are $10\times$ and $4\times$ faster respectively while maintaining a comparable storage requirement and high quality reconstruction. Moreover, the FPS of 4DGS-1K far exceeds the current state-of-the-art levels. It is nearly twice as fast as the current fastest model, Dynamic 3DGS [23] while requiring only **1%** of the storage size. Additionally, 4DGS-1K achieves better visual quality than that of Dynamic 3DGS [23], with an increase of about $1.2dB$ in PSNR. Compared to the storage-efficient model, E-D3DGS [3] and DyNeRF [18] we achieve an increase of over $0.5dB$ in PSNR and fast rendering speed. Fig. 5 offers qualitative comparisons for the Sear Steak, demonstrating that our results contain more vivid details.

Comparisons on synthetic dataset. In our experiments, we benchmarked 4DGS-1K against several baselines using the monocular synthetic dataset introduced by D-NeRF [30]. The result is shown in Tab. 2. Compared to 4DGS [40], our method achieves up to $40\times$ compression and $4\times$ faster rendering speed. It is worth noting that the rendering quality of our model even surpasses that of the original 4DGS, with an increase of about $0.38dB$ in PSNR. Furthermore, our approach exhibits higher rendering quality and smaller storage overhead compared to most Gaussian-based methods. We provide qualitative results in Fig. 5 for a more visual assessment.

5.3. Ablation Study

To evaluate the contribution of each component and the effectiveness of the pruning strategy for temporal filtering, we conducted ablation experiments on the N3V dataset [18]. More ablations are provided in the supplement(See Sec. 8).

Table 4. **Ablation study of Spatial-Temporal Variation Score.** We compare our Spatial-Temporal Variation Score with other variants, and report the PSNR score of each scene.

ID	Model	Sear Steak	Flame Salmon
a	4DGS w/o Prune	33.60	29.10
b	\mathcal{S}_i^S Only	33.62	28.75
c	\mathcal{S}_i^T Only	33.59	28.79
d	\mathcal{S}_i (w. $p_i^{(1)}(t)$)	33.67	28.81
e	\mathcal{S}_i (w. Σ_t)	33.47	28.71
f	Ours	33.76	28.90

Pruning. As shown in Tab. 3, our pruning strategy reduces the number of Gaussians by 80%, and achieves $5\times$ compression ratio and $5\times$ faster rasterization speed while slightly improving rendering quality. As shown in Fig. 2a, our pruning strategy also reduces the presence of Gaussians with short lifespan. As such, 4DGS-1k processes far fewer unnecessary Gaussians (See Fig. 2b) during rendering.

Furthermore, we compare our Spatial-Temporal Variation Score with several variants. Specific settings are described in Sec. 8. As shown in Tab. 4, using spatial and temporal scores separately reduce the PSNR. This occurs because separate scores can amplify extreme Gaussians. For instance, using only the spatial score (b) may retain Gaussians that cover just a single frame but occupy a large spatial volume. Our combined score balances these factors. For variant d, using the first derivative may cause some small Gaussians to have large \mathcal{S}_i^T compared to ours. Moreover, since most Gaussians have small Σ_t , it is difficult to distinguish them by using Σ_t along (See e). Moreover, as shown in Fig. 2c, the pruning process expands the range of adjacent frames. It allows larger intervals for the temporal filter. We will discuss it in the next part.

Temporal Filtering. As illustrated in Tab. 3, the results of b and c are obtained by directly applying the filter to 4DGS without fine-tuning. It proves that this component can enhance the rendering speed of 4DGS. However, as mentioned in Sec. 4.1, the 4DGS contains a huge number of short lifespan Gaussians. It results in some Gaussians being overlooked in the filter, causing a slight decrease in rendering quality. However, through pruning, most Gaussians are ensured to have long lifespan, making them visible even at large intervals. Therefore, it alleviates the issue of Gaussians being overlooked (See f). Furthermore, appropriate fine-tuning allows the Gaussians in the active Gaussians list to relearn the scene features to compensate for the loss incurred by the temporal filter (See e and f).

6. Conclusion

In this paper, we present **4DGS-1K**, a compact and memory-efficient dynamic scene representation capable of running at over 1000 FPS on modern GPUs. We introduce a novel pruning criterion called the spatial-temporal variation score, which eliminates a significant number of redundant Gaussian points in 4DGS, drastically reducing storage requirements. Additionally, we propose a temporal filter that selectively activates only a subset of Gaussians during each frame’s rendering. This approach enables our rendering speed to far surpass that of existing baselines. Compared to vanilla 4DGS, 4DGS-1K achieves a $41\times$ reduction in storage and $9\times$ faster rasterization speed while maintaining high-quality reconstruction.

1000+ FPS 4D Gaussian Splatting for Dynamic Scene Rendering

Supplementary Material

The Supplementary material is organized as follows:

- Sec. 7: provides additional visualization results and quantitative results. Furthermore, it also shows the resource consumption which reveals the potential of 4DGS-1K for deployment on low-performance hardware.
- Sec. 8: provides additional ablation study. It firstly provides the variant settings in the main text, then it presents more additional ablation study to illustrate that our parameter selection is the result of a trade-off between rendering quality and storage size.
- Sec. 9: discusses the reason of improved performance for 4DGS-1K. Furthermore, we introduce the limitations and potential future directions of 4DGS-1K.

7. Experimental Results

7.1. Per scene result

We provide per-scene quantitative comparisons on the N3V Dataset [18](Tab. 5) and D-NeRF Dataset [30](Tab. 6). Compared to vanilla 4DGS [40], our model significantly reduces the storage requirements and enhances rendering speed while maintaining high-quality reconstruction. Fig. 12 and Fig. 13 show more visual comparisons on the N3V Dataset. Fig. 14, Fig. 15 and Fig. 16 show visual comparisons on the D-NeRF Dataset.

7.2. Resource consumption

We present the resource consumption metrics, including training time, GPU memory allocation and additional storage space. On the N3V dataset [18], 4DGS-1K only takes approximately 30 minutes to fine-tune, with GPU memory allocation of 10.54GB. During rendering, it only consumes 1.62GB of GPU memory. For storage requirement, 4DGS-1K requires additional storage for the mask of filter and codebook; however, these occupy only a minimal portion of the total storage, approximately 1 MB per scene. These parts are also included in the final experiment results.

The above results demonstrate the potential of 4DGS-1K for deployment on low-performance hardware. Consequently, we further test 4DGS-1K on TITAN X GPU, where 4DGS-1K maintains 200+ FPS on the N3V dataset, still far outperforming vanilla 4DGS (20 FPS).

7.3. Additional experiments for redundancy

In this section, we provide additional experiments for redundancy study as a supplement to Sec. 4.1. It is composed of two parts: first, the visualization of the Gaussian with short lifespan distribution, and secondly, the relationship between FPS and the number of inactive Gaussians.

Visualization of Gaussians with small lifespan. In Sec. 4.1, we argue that in vanilla 4DGS, nearly all Gaussians have a short lifespan, especially around the edge of fast-moving objects. Therefore, we visualize the spatial distribution of Σ_t to better support our redundancy study in Sec. 4.1.

Specifically, we visualize the distribution of Σ_t at several timestamps in *Sear Steak* Scene. The visualization results are shown in Fig. 6. For visualization, we take the reciprocal of Σ_t during rendering and then normalize it. Therefore, brighter regions in the rendered image indicate smaller Σ_t .

As shown in Fig. 6, Gaussians with short lifespan are primarily concentrated in regions of object motion, such as the moving person and dog. Moreover, we observe that Gaussians with small Σ_t also appear on the edges of some objects which exhibit significant color variation. This is because small Gaussians are preferred in these regions to capture the high-frequency details in the spatial dimension. As vanilla 4DGS [40] treats time and space dimensions equally, these Gaussians also have short lifespan in the temporal dimension.

Relationship between FPS and the number of inactive Gaussians. In Sec. 4.1, our primary prior assumption is that the number of inactive Gaussians affects the FPS. Therefore, we visualize the relationship between FPS and the number of inactive Gaussians.

However, only limiting the total number of Gaussians is incorrect in this task. As the total number increases, the number of active Gaussians and inactive Gaussians also increases, which cannot clarify whether the FPS variation is caused by active or inactive Gaussians. Consequently, we first identify the active Gaussians by rendering and then add a amount of inactive Gaussians among these Gaussians.

We visualize the result in the *Sear Steak* Scene(See Fig. 7). The FPS decreases as the number of inactive Gaussians increases. This phenomenon strongly supports our redundancy study in Sec. 4.1.

7.4. Visualizations of Pruned Gaussians

We provide the visualization of pruned Gaussians in the *Sear Steak* Scene, as shown in Fig. 8. Our pruning strategy can accurately identify Gaussians with short lifespan(See Fig. 8c) while maintaining the high quality reconstruction(See Fig. 8d). The quantized results after pruning are presented in Tab. 3. Our pruning technique achieves $5\times$ compression ratio and $5\times$ faster rasterization speed while slightly improving rendering quality.

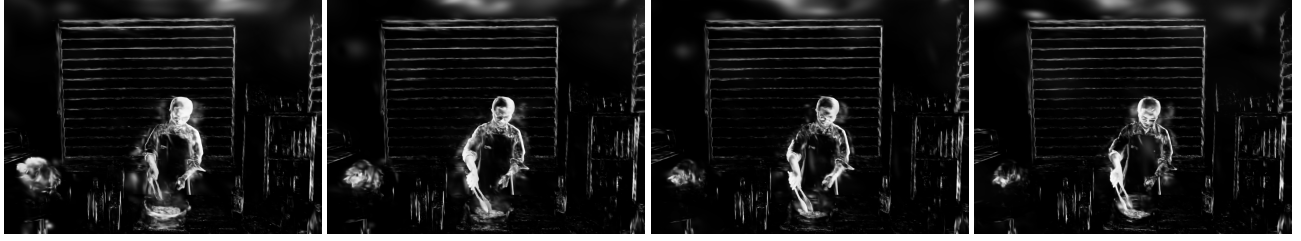


Figure 6. **Visualizations of Distribution of Σ_t .**

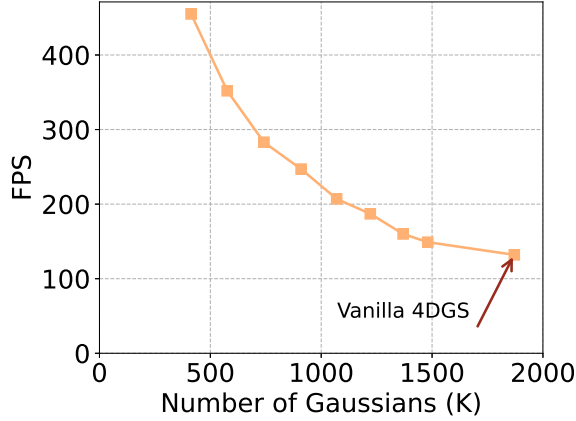


Figure 7. **Relationship between rendering speed and the number of inactive Gaussians.**

7.5. Video result

In this work, we propose a novel framework for dynamic 3D reconstruction. Therefore, we provide several videos that are rendered from testing viewpoints on the N3V datasets and D-NeRF datasets to show the reconstruction quality and temporal consistency of 4DGS-1K. These videos are composed by concatenating each frame of 4DGS and our method.

8. Additional ablation study

In this section, we firstly provide the variant settings of Tab. 4. Furthermore, in addition to the ablation study in the main text, we also investigate the impact of the pruning ratio and different key-frames intervals on rendering quality. We select three distinct scenes, *Cook Spinach*, *Cut Roasted Beef*, and *Sear Steak* on the N3V dataset [18] due to the varying performance across different scenes resulting from their unique characteristics. These results show that our default configuration is a well-rounded choice for a wide range of scenes.

Variant Settings. As described in Sec. 4.2.1, our Spatial-Temporal Variation Score is composed of two parts, *spatial score* that measures the Gaussians contributions to the pix-

els in rendering, and *temporal score* considering the lifespan of Gaussians. By aggregating both spatial and temporal score, our score \mathcal{S}_i can be written as:

$$\mathcal{S}_i = \sum_{t=0}^T \mathcal{S}_i^T \mathcal{S}_i^S \quad (8)$$

Therefore, the variant scores in Tab. 4 can be written as follow.

- (b) \mathcal{S}_i^S Only: only considering the spatial part of our score. It can be written as:

$$\mathcal{S}_i = \sum_{t=0}^T \mathcal{S}_i^S \quad (9)$$

- (c) \mathcal{S}_i^T Only: only considering the temporal contribution part of our score. It can be written as:

$$\mathcal{S}_i = \sum_{t=0}^T \mathcal{S}_i^T \quad (10)$$

- (b) \mathcal{S}_i (w. $p_i^{(1)}(t)$): Replace the $p_i^{(2)}(t)$ with $p_i^{(1)}(t)$ in temporal score \mathcal{S}_i^T . It can be written as:

$$\begin{aligned} \mathcal{S}_i &= \sum_{t=0}^T \mathcal{S}_i^T \mathcal{S}_i^S \\ &= \sum_{t=0}^T \mathcal{S}_i^{TV} \gamma(\mathcal{S}_i^{4D}) \mathcal{S}_i^S \\ &= \sum_{t=0}^T \frac{1}{0.5 \cdot \tanh(|p_i^{(1)}(t)|) + 0.5} \gamma(\mathcal{S}_i^{4D}) \mathcal{S}_i^S. \end{aligned} \quad (11)$$

- (c) \mathcal{S}_i (w. Σ_t) Replace the \mathcal{S}_i^{TV} with Σ_t . It can be written as:

$$\begin{aligned} \mathcal{S}_i &= \sum_{t=0}^T \mathcal{S}_i^T \mathcal{S}_i^S \\ &= \sum_{t=0}^T \Sigma_t \gamma(\mathcal{S}_i^{4D}) \mathcal{S}_i^S \end{aligned} \quad (12)$$

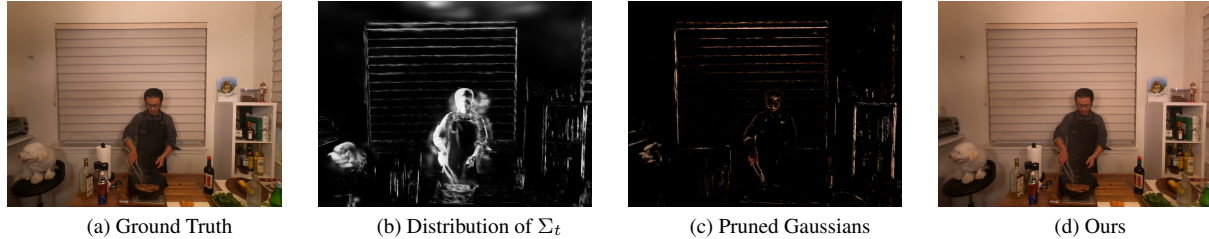


Figure 8. Visualization of Pruned Gaussians.

Performance change with pruning ratio. As illustrated in Fig. 10, we analyze the relationship between the pruning ratio and rendering quality. This reveals that our spatial-temporal variation score based pruning can even improve scene rendering quality when the pruning ratio is relatively low in the *Cook Spinach* and *Sear Steak* scenes. Moreover, at higher thresholds, it can maintain results comparable to the vanilla 4DGS [40]. Our default setting represents a balanced trade-off between rendering quality and storage size. This setting allows us to achieve a $5\times$ compression ratio while still maintaining high-quality reconstruction.

Performance change with key-frames intervals. As shown in Fig. 11, although the temporal filter effectively improves rendering speed, its performance degrades significantly when the filter is with long-interval keyframes. However, by integrating the temporal filter into the fine-tuning process, this limitation can be mitigated. The fundamental reason is that some Gaussians which may carry critical scene information are being overlooked due to overly long intervals. However, the fine-tuning process effectively compensates for the loss of this portion of information. This allows us to utilize longer intervals to reduce the additional computational overhead caused by mask calculations.

9. Discussion

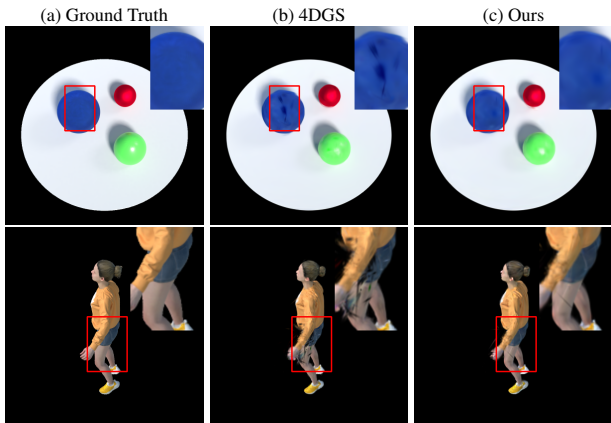


Figure 9. Visualization of improved performance.

Improved performance. As shown in Tab. 2, our model achieves a slight PSNR improvement on the D-NeRF Dataset [30]. This is because vanilla 4DGS often suffers from floaters and artifacts, due to the limited training viewpoints on the D-NeRF Datasets. However, in our study, 4DGS-1K not only can prune the Gaussians with short lifespan, but also reduce the occurrence of floaters and artifacts, as shown in Fig. 9. We visualize two scenes, *Bouncingballs* and *Jumpingjacks*, on the D-NeRF Dataset. These two scenes exhibit floaters and artifacts issues due to limited training viewpoints, as shown in the red box. However, this issue does not appear in 4DGS-1K. Through pruning and filtering, 4DGS-1K successfully mitigates the occurrence of this phenomenon.

Limitations and Future work. As shown in Tab. 5 and Tab. 6, due to the acceleration provided by the temporal filter, the proportion of time spent on the rasterization process sharply decreases relative to the total rendering time. Therefore, the time consumed by preliminary preparation stages has not gradually become negligible. We hope that future work will focus on optimizing these additional operations within the rendering module to improve its computational performance. Moreover, during the pruning process, we specified a predefined pruning ratio. This pruning ratio is influenced by the inherent characteristics of the scene. As shown in Fig. 10, an improper pruning ratio will cause a sharp drop in rendering quality. Therefore, identifying the minimal number of Gaussians required to maintain high-quality rendering across different scenes remains a challenge. Lastly, there is a significant amount of existing work on Gaussian-based novel view synthesis for dynamic scenes, whereas our model is specifically tailored to a particular model, 4DGS [40]. Therefore, developing a universal compression method for these Gaussian-based models is a promising direction for subsequent research endeavors.

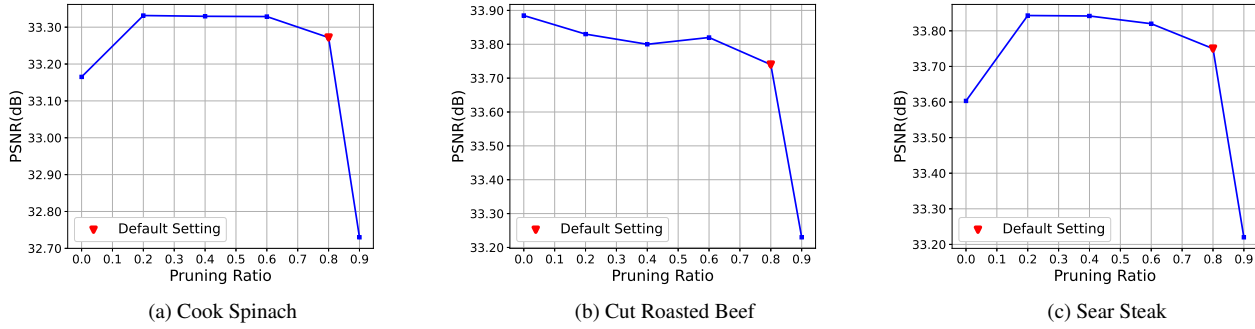


Figure 10. Rate-distortion curves evaluated on diverse scenes with different pruning ratios.

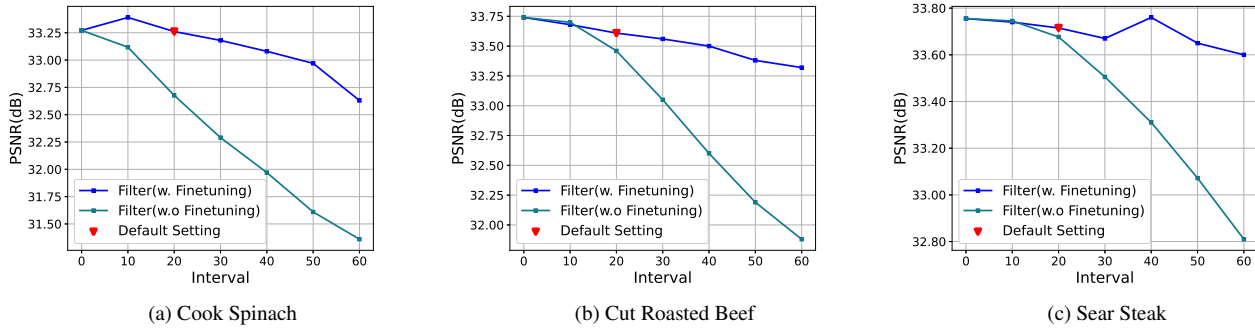


Figure 11. Rate-distortion curves evaluated on diverse scenes with different key-frames interval.

Table 5. Per-scene results of N3V datasets.

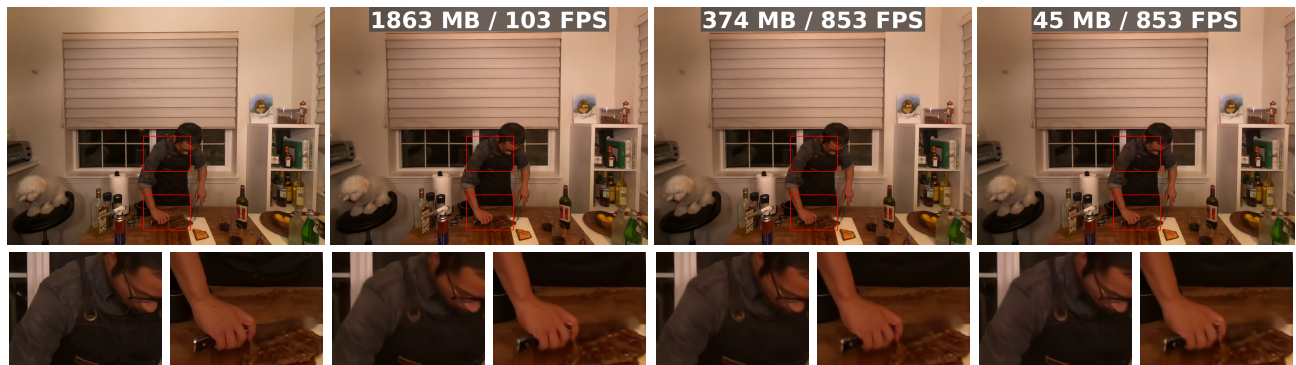
Scene		Coffee Martini	Cook Spinach	Cut Roasted Beef	Flame Salmon	Flame Steak	Sear Steak	Average
4DGS	PSNR	27.9286	33.1651	33.8849	29.1009	33.7970	33.6031	31.9133
	SSIM	0.9160	0.9545	0.9589	0.9236	0.9615	0.9607	0.9459
	LPIPS	0.0759	0.0449	0.0408	0.0691	0.0383	0.0418	0.0518
	Storage(MB)	2764	2211	1863	2969	1536	1167	2085
	FPS	43	89	103	31	122	152	90
	Raster FPS	75	103	122	70	148	195	118
	#NUM	4441271	3530165	2979832	4719443	2457356	1870891	3333160
Ours	PSNR	28.5780	33.2613	33.6092	28.8488	33.2804	33.7150	31.8821
	SSIM	0.9185	0.9553	0.9570	0.9221	0.9598	0.9615	0.9457
	LPIPS	0.0726	0.0459	0.0435	0.0707	0.0417	0.0401	0.0524
	Storage(MB)	557.4	443.11	374.05	592.4	308.4	234.8	418.36
	FPS	696	803	853	680	864	935	805
	Raster FPS	901	1088	1163	879	1189	1332	1092
	#NUM	888254	706033	595967	943889	491471	374178	666632
Ours-PP	PSNR	28.5472	33.0641	33.7767	28.9878	33.2519	33.6053	31.8722
	SSIM	0.9166	0.9540	0.9562	0.9209	0.9581	0.9604	0.9444
	LPIPS	0.0744	0.0467	0.0445	0.0712	0.0421	0.0402	0.0532
	Storage(MB)	64.94	52.04	44.54	69.24	36.94	29.34	49.50
	FPS	696	803	853	680	864	935	805
	Raster FPS	901	1088	1163	879	1189	1332	1092
	#NUM	888254	706033	595967	943889	491471	374178	666632



(a) Results on Coffee Martini Scene.



(b) Results on Cook Spinach Scene.

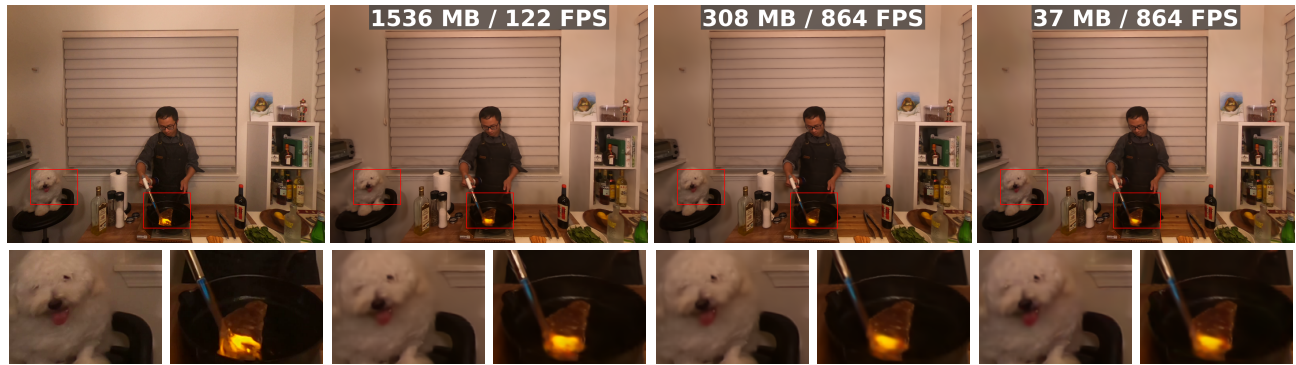


(c) Results on Cut Roasted Beef Scene.

Figure 12. Qualitative comparisons of 4DGS and our method on the N3V dataset. To be continued in the next page.



(a) Results on Flame Salmon Scene.

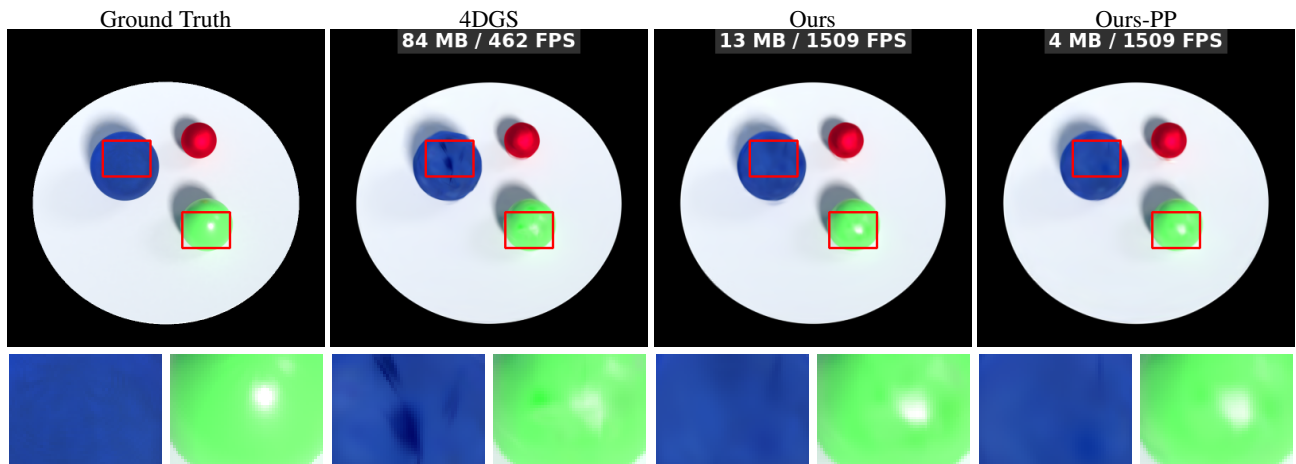


(b) Results on Flame Steak Scene.



(c) Results on Sear Steak Scene.

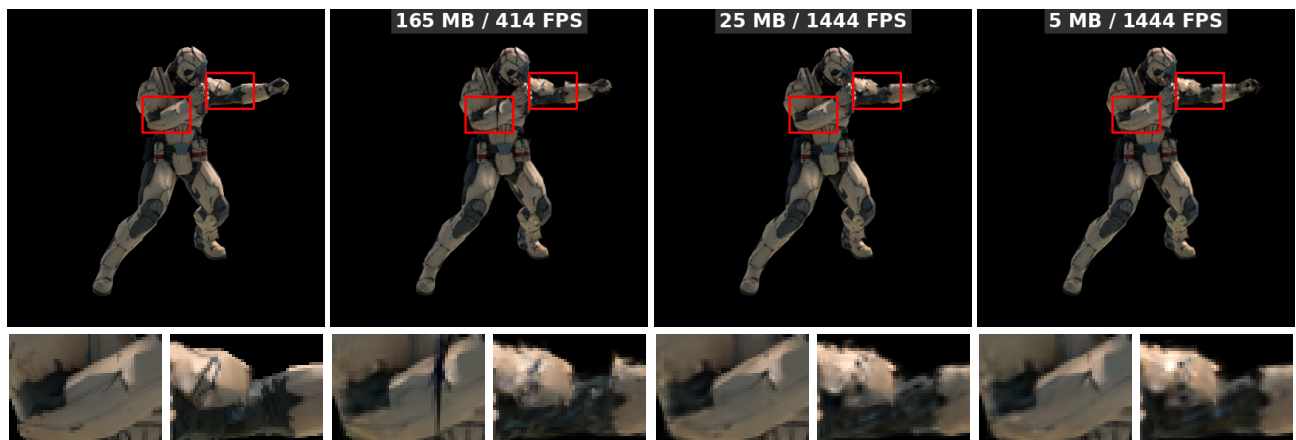
Figure 13. Qualitative comparisons of 4DGS and our method on the N3V dataset.



(a) Results on Bouncingballs Scene.

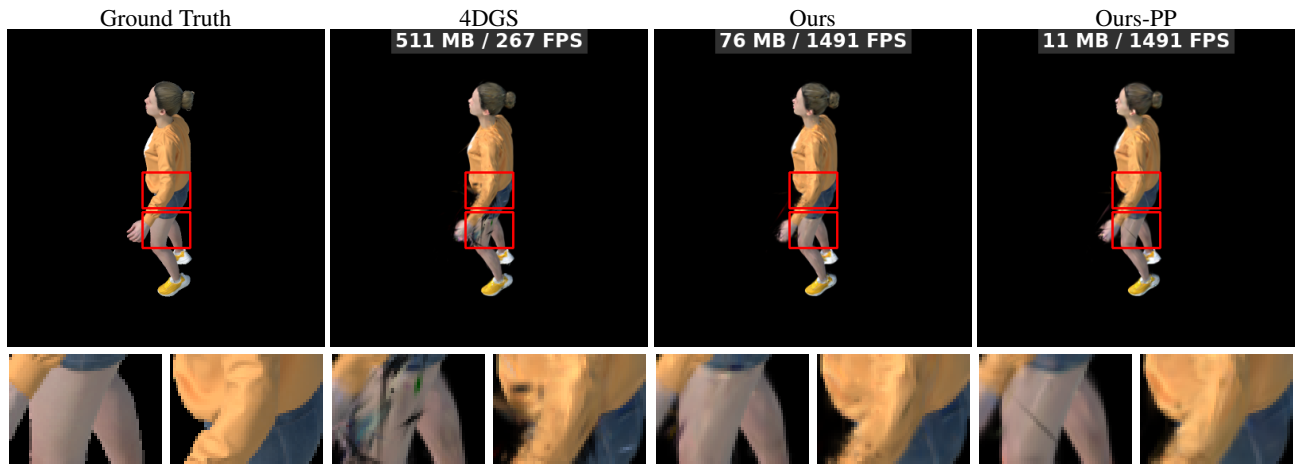


(b) Results on Hellwarrior Scene.

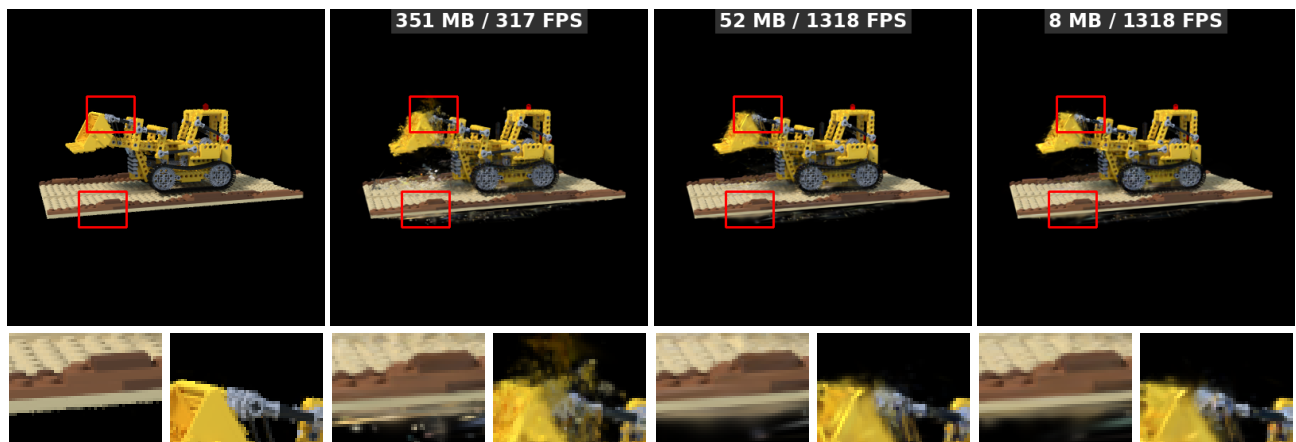


(c) Results on Hook Scene.

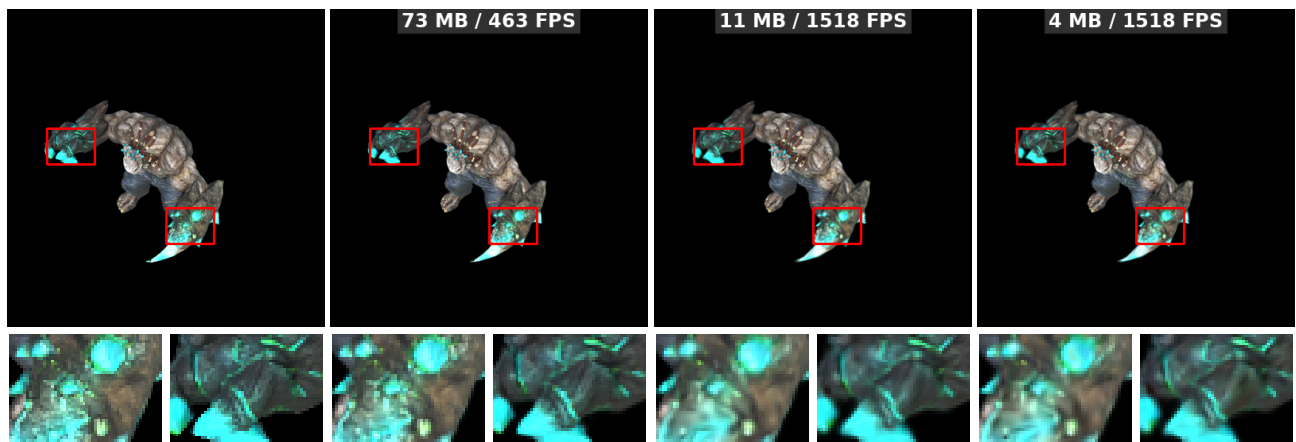
Figure 14. Qualitative comparisons of 4DGS and our method on the D-nerf dataset. To be continued in the next page.



(a) Results on Jumpingjacks Scene.

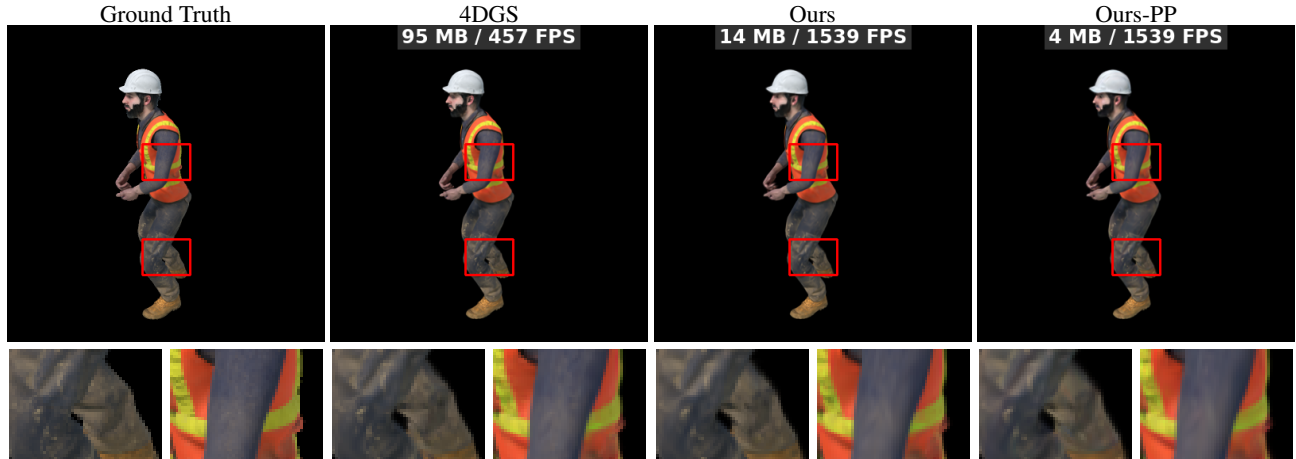


(b) Results on Lego Scene.

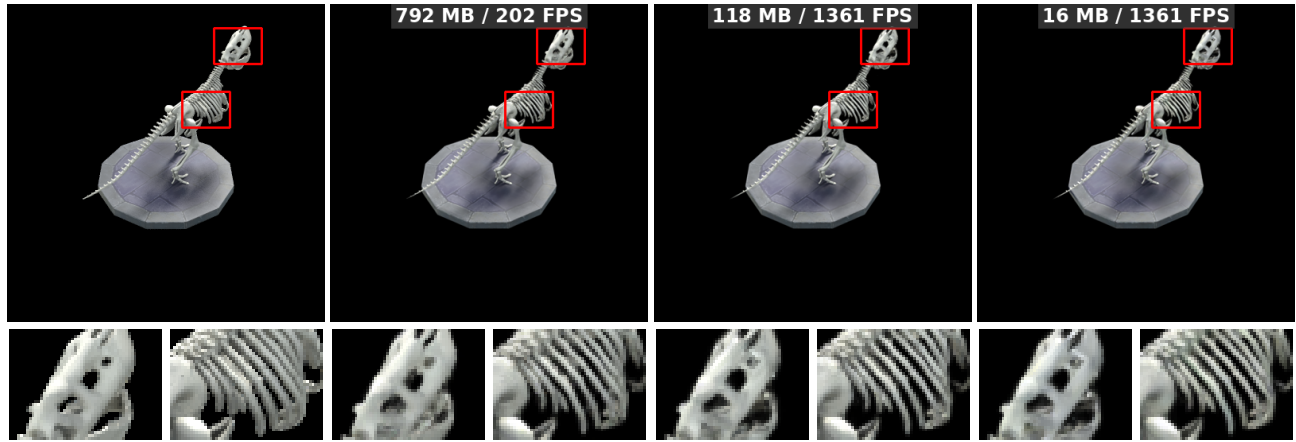


(c) Results on Mutant Scene.

Figure 15. Qualitative comparisons of 4DGS and our method on the D-nerf dataset. To be continued in the next page.



(a) Results on Standup Scene.



(b) Results on Trex Scene.

Figure 16. Qualitative comparisons of 4DGS and our method on the D-nerf dataset.

Table 6. Per-scene results of D-NeRF datasets.

Scene	Bouncingballs	Hellwarrior	Hook	Jumpingjacks	Lego	Mutant	Standup	Trex	Average	
4DGS	PSNR	33.3472	34.7296	31.9369	30.8247	25.3320	38.9257	39.0411	29.8542	32.9989
	SSIM	0.9821	0.9516	0.9635	0.9684	0.9178	0.9903	0.9896	0.9795	0.9678
	LPIPS	0.0252	0.0652	0.0385	0.0340	0.0819	0.0090	0.0094	0.0193	0.0353
	Storage(MB)	83.69	156.53	164.91	510.99	351.19	73.24	95.38	791.66	278.45
	FPS	462	426	414	267	317	463	457	202	376
	Raster FPS	1951	1433	1309	489	634	1861	1878	302	1232
	#NUM	133762	250201	263593	816773	561357	117062	152454	1265408	445076
Ours	PSNR	33.4532	35.0316	32.5118	31.8045	26.8319	37.1916	39.3990	30.4726	33.3370
	SSIM	0.9826	0.9530	0.9653	0.9716	0.9280	0.9886	0.9896	0.9811	0.9699
	LPIPS	0.0248	0.0644	0.035	0.0322	0.0674	0.0124	0.0099	0.0180	0.0330
	Storage(MB)	12.56	23.38	24.63	76.19	52.45	10.97	14.25	118.24	41.58
	FPS	1509	1517	1444	1491	1318	1518	1539	1361	1462
	Raster FPS	2600	2665	2634	2476	2067	2598	2644	2174	2482
	#NUM	20065	37368	39360	121776	83837	17527	22768	188986	66460
Ours-PP	PSNR	33.4592	35.1570	32.5498	31.8467	27.2850	37.0218	39.0713	30.6063	33.3746
	SSIM	0.9821	0.9537	0.9671	0.9728	0.9315	0.9883	0.9896	0.9821	0.9709
	LPIPS	0.0259	0.0629	0.0345	0.0309	0.0646	0.0139	0.0109	0.0173	0.0326
	Storage(MB)	4.12	5.29	5.39	11.04	8.48	3.56	3.88	16.11	7.23
	FPS	1509	1517	1444	1491	1318	1518	1539	1361	1462
	Raster FPS	2600	2665	2634	2476	2067	2598	2644	2174	2482
	#NUM	20065	37368	39360	121776	83837	17527	22768	188986	66460

References

- [1] Muhammad Salman Ali, Maryam Qamar, Sung-Ho Bae, and Enzo Tartaglione. Trimming the fat: Efficient compression of 3d gaussian splats through pruning. *arXiv preprint arXiv:2406.18214*, 2024. [3](#)
- [2] Benjamin Attal, Jia-Bin Huang, Christian Richardt, Michael Zollhoefer, Johannes Kopf, Matthew O’Toole, and Changil Kim. Hyperreel: High-fidelity 6-dof video with ray-conditioned sampling. In *Proceedings of the IEEE/CVF Conference on Computer Vision and Pattern Recognition*, pages 16610–16620, 2023. [1](#), [2](#), [6](#), [7](#)
- [3] Jeongmin Bae, Seoha Kim, Youngsik Yun, Hahyun Lee, Gun Bang, and Youngjung Uh. Per-gaussian embedding-based deformation for deformable 3d gaussian splatting. *arXiv preprint arXiv:2404.03613*, 2024. [2](#), [6](#), [7](#), [8](#)
- [4] Ang Cao and Justin Johnson. Hexplane: A fast representation for dynamic scenes. In *Proceedings of the IEEE/CVF Conference on Computer Vision and Pattern Recognition*, pages 130–141, 2023. [2](#)
- [5] Anpei Chen, Zexiang Xu, Andreas Geiger, Jingyi Yu, and Hao Su. Tensorf: Tensorial radiance fields. In *European conference on computer vision*, pages 333–350. Springer, 2022. [2](#)
- [6] Devikalyan Das, Christopher Wewer, Raza Yunus, Eddy Ilg, and Jan Eric Lenssen. Neural parametric gaussians for monocular non-rigid object reconstruction. In *Proceedings of the IEEE/CVF Conference on Computer Vision and Pattern Recognition*, pages 10715–10725, 2024. [2](#)
- [7] Yuanxing Duan, Fangyin Wei, Qiyu Dai, Yuhang He, Wenzheng Chen, and Baoquan Chen. 4d-rotor gaussian splatting: towards efficient novel view synthesis for dynamic scenes. In *ACM SIGGRAPH 2024 Conference Papers*, pages 1–11, 2024. [6](#)
- [8] Zhiwen Fan, Kevin Wang, Kairun Wen, Zehao Zhu, Dejia Xu, and Zhangyang Wang. Lightgaussian: Unbounded 3d gaussian compression with 15x reduction and 200+ fps. *arXiv preprint arXiv:2311.17245*, 2023. [3](#), [4](#), [5](#)
- [9] Guangchi Fang and Bing Wang. Mini-splatting: Representing scenes with a constrained number of gaussians. *arXiv preprint arXiv:2403.14166*, 2024. [3](#), [4](#)
- [10] Jiemin Fang, Taoran Yi, Xinggang Wang, Lingxi Xie, Xiaopeng Zhang, Wenyu Liu, Matthias Nießner, and Qi Tian. Fast dynamic radiance fields with time-aware neural voxels. In *SIGGRAPH Asia 2022 Conference Papers*, pages 1–9, 2022. [6](#)
- [11] Sara Fridovich-Keil, Alex Yu, Matthew Tancik, Qin-hong Chen, Benjamin Recht, and Angjoo Kanazawa. Plenoxels: Radiance fields without neural networks. In *Proceedings of the IEEE/CVF conference on computer vision and pattern recognition*, pages 5501–5510, 2022. [2](#)
- [12] Sara Fridovich-Keil, Giacomo Meanti, Frederik Rahbæk Warburg, Benjamin Recht, and Angjoo Kanazawa. K-planes: Explicit radiance fields in space, time, and appearance. In *Proceedings of the IEEE/CVF Conference on Computer Vision and Pattern Recognition*, pages 12479–12488, 2023. [1](#), [2](#), [6](#), [7](#)
- [13] Zhiyang Guo, Wengang Zhou, Li Li, Min Wang, and Houqiang Li. Motion-aware 3d gaussian splatting for efficient dynamic scene reconstruction. *arXiv preprint arXiv:2403.11447*, 2024. [2](#)
- [14] Bernhard Kerbl, Georgios Kopanas, Thomas Leimkühler, and George Drettakis. 3d gaussian splatting for real-time radiance field rendering. *ACM Trans. Graph.*, 42(4):139–1, 2023. [2](#), [3](#), [4](#)
- [15] Alex Krizhevsky, Ilya Sutskever, and Geoffrey E Hinton. Imagenet classification with deep convolutional neural networks. *Advances in neural information processing systems*, 25, 2012. [6](#)
- [16] Joo Chan Lee, Daniel Rho, Xiangyu Sun, Jong Hwan Ko, and Eunbyung Park. Compact 3d gaussian representation for radiance field. In *Proceedings of the IEEE/CVF Conference on Computer Vision and Pattern Recognition*, pages 21719–21728, 2024. [3](#), [6](#), [8](#)
- [17] Lingzhi Li, Zhen Shen, Zhongshu Wang, Li Shen, and Ping Tan. Streaming radiance fields for 3d video synthesis. *Advances in Neural Information Processing Systems*, 35:13485–13498, 2022. [2](#), [6](#), [7](#)
- [18] Tianye Li, Mira Slavcheva, Michael Zollhoefer, Simon Green, Christoph Lassner, Changil Kim, Tanner Schmidt, Steven Lovegrove, Michael Goesele, Richard Newcombe, et al. Neural 3d video synthesis from multi-view video. In *Proceedings of the IEEE/CVF Conference on Computer Vision and Pattern Recognition*, pages 5521–5531, 2022. [1](#), [2](#), [6](#), [7](#), [8](#), [9](#), [10](#)
- [19] Zhan Li, Zhang Chen, Zhong Li, and Yi Xu. Space-time gaussian feature splatting for real-time dynamic view synthesis. In *Proceedings of the IEEE/CVF Conference on Computer Vision and Pattern Recognition*, pages 8508–8520, 2024. [6](#), [7](#)
- [20] Wenkai Liu, Tao Guan, Bin Zhu, Lili Ju, Zikai Song, Dan Li, Yuesong Wang, and Wei Yang. Efficientgts: Streamlining gaussian splatting for large-scale high-resolution scene representation. *arXiv preprint arXiv:2404.12777*, 2024. [3](#)
- [21] Stephen Lombardi, Tomas Simon, Jason Saragih, Gabriel Schwartz, Andreas Lehrmann, and Yaser Sheikh. Neural volumes: Learning dynamic ren-

- derable volumes from images. *arXiv preprint arXiv:1906.07751*, 2019. 1, 2, 6, 7
- [22] Zhicheng Lu, Xiang Guo, Le Hui, Tianrui Chen, Min Yang, Xiao Tang, Feng Zhu, and Yuchao Dai. 3d geometry-aware deformable gaussian splatting for dynamic view synthesis. In *Proceedings of the IEEE/CVF Conference on Computer Vision and Pattern Recognition*, pages 8900–8910, 2024. 2
- [23] Jonathon Luiten, Georgios Kopanas, Bastian Leibe, and Deva Ramanan. Dynamic 3d gaussians: Tracking by persistent dynamic view synthesis. *arXiv preprint arXiv:2308.09713*, 2023. 6, 7, 8
- [24] Ben Mildenhall, Pratul P Srinivasan, Rodrigo Ortiz-Cayon, Nima Khademi Kalantari, Ravi Ramamoorthi, Ren Ng, and Abhishek Kar. Local light field fusion: Practical view synthesis with prescriptive sampling guidelines. *ACM Transactions on Graphics (ToG)*, 38(4):1–14, 2019. 2
- [25] Ben Mildenhall, Pratul P Srinivasan, Matthew Tancik, Jonathan T Barron, Ravi Ramamoorthi, and Ren Ng. Nerf: Representing scenes as neural radiance fields for view synthesis. *Communications of the ACM*, 65(1):99–106, 2021. 1, 2
- [26] Thomas Müller, Alex Evans, Christoph Schied, and Alexander Keller. Instant neural graphics primitives with a multiresolution hash encoding. *ACM transactions on graphics (TOG)*, 41(4):1–15, 2022. 2
- [27] KL Navaneet, Kossar Pourahmadi Meibodi, Soroush Abbasi Koohpayegani, and Hamed Pirsiavash. Compgs: Smaller and faster gaussian splatting with vector quantization. In *European Conference on Computer Vision*, 2024. 3, 7
- [28] Michael Niemeyer, Fabian Manhardt, Marie-Julie Rakotosaona, Michael Oechsle, Daniel Duckworth, Rama Gosula, Keisuke Tateno, John Bates, Dominik Kaeser, and Federico Tombari. Radsplat: Radiance field-informed gaussian splatting for robust real-time rendering with 900+ fps. *arXiv preprint arXiv:2403.13806*, 2024. 3
- [29] Panagiotis Papantonakis, Georgios Kopanas, Bernhard Kerbl, Alexandre Lanvin, and George Drettakis. Reducing the memory footprint of 3d gaussian splatting. *Proceedings of the ACM on Computer Graphics and Interactive Techniques*, 7(1):1–17, 2024. 3
- [30] Albert Pumarola, Enric Corona, Gerard Pons-Moll, and Francesc Moreno-Noguer. D-nerf: Neural radiance fields for dynamic scenes. In *Proceedings of the IEEE/CVF Conference on Computer Vision and Pattern Recognition*, pages 10318–10327, 2021. 2, 6, 7, 8, 9, 11
- [31] Christian Reiser, Songyou Peng, Yiyi Liao, and Andreas Geiger. Kilonerf: Speeding up neural radiance fields with thousands of tiny mlps. In *Proceedings of the IEEE/CVF international conference on computer vision*, pages 14335–14345, 2021. 2
- [32] Katja Schwarz, Axel Sauer, Michael Niemeyer, Yiyi Liao, and Andreas Geiger. Voxgraf: Fast 3d-aware image synthesis with sparse voxel grids. *Advances in Neural Information Processing Systems*, 35:33999–34011, 2022. 2
- [33] Karen Simonyan and Andrew Zisserman. Very deep convolutional networks for large-scale image recognition. *arXiv preprint arXiv:1409.1556*, 2014. 6
- [34] Liangchen Song, Anpei Chen, Zhong Li, Zhang Chen, Lele Chen, Junsong Yuan, Yi Xu, and Andreas Geiger. Nerfplayer: A streamable dynamic scene representation with decomposed neural radiance fields. *IEEE Transactions on Visualization and Computer Graphics*, 29(5):2732–2742, 2023. 2
- [35] Cheng Sun, Min Sun, and Hwann-Tzong Chen. Direct voxel grid optimization: Super-fast convergence for radiance fields reconstruction. In *Proceedings of the IEEE/CVF conference on computer vision and pattern recognition*, pages 5459–5469, 2022. 2
- [36] Feng Wang, Sinan Tan, Xinghang Li, Zeyue Tian, Yafei Song, and Huaping Liu. Mixed neural voxels for fast multi-view video synthesis. In *Proceedings of the IEEE/CVF International Conference on Computer Vision*, pages 19706–19716, 2023. 2
- [37] Huan Wang, Jian Ren, Zeng Huang, Kyle Olszewski, Menglei Chai, Yun Fu, and Sergey Tulyakov. R2l: Distilling neural radiance field to neural light field for efficient novel view synthesis. In *European Conference on Computer Vision*, pages 612–629. Springer, 2022. 2
- [38] Liao Wang, Jiakai Zhang, Xinhang Liu, Fuqiang Zhao, Yanshun Zhang, Yingliang Zhang, Minye Wu, Jingyi Yu, and Lan Xu. Fourier plenotrees for dynamic radiance field rendering in real-time. In *Proceedings of the IEEE/CVF Conference on Computer Vision and Pattern Recognition*, pages 13524–13534, 2022. 2
- [39] Guanjun Wu, Taoran Yi, Jiemin Fang, Lingxi Xie, Xiaopeng Zhang, Wei Wei, Wenyu Liu, Qi Tian, and Xinggang Wang. 4d gaussian splatting for real-time dynamic scene rendering. In *Proceedings of the IEEE/CVF Conference on Computer Vision and Pattern Recognition*, pages 20310–20320, 2024. 2, 6, 7
- [40] Zeyu Yang, Hongye Yang, Zijie Pan, and Li Zhang. Real-time photorealistic dynamic scene representation and rendering with 4d gaussian splatting. *arXiv preprint arXiv:2310.10642*, 2023. 1, 2, 3, 5, 6, 7, 8, 9, 11
- [41] Ziyi Yang, Xinyu Gao, Wen Zhou, Shaohui Jiao, Yuqing Zhang, and Xiaogang Jin. Deformable 3d gaussians for high-fidelity monocular dynamic scene

- reconstruction. In *Proceedings of the IEEE/CVF Conference on Computer Vision and Pattern Recognition*, pages 20331–20341, 2024. 2, 6
- [42] Richard Zhang, Phillip Isola, Alexei A Efros, Eli Shechtman, and Oliver Wang. The unreasonable effectiveness of deep features as a perceptual metric. In *Proceedings of the IEEE conference on computer vision and pattern recognition*, pages 586–595, 2018. 6
- [43] Xinjie Zhang, Zhening Liu, Yifan Zhang, Xingtong Ge, Dailan He, Tongda Xu, Yan Wang, Zehong Lin, Shuicheng Yan, and Jun Zhang. Mega: Memory-efficient 4d gaussian splatting for dynamic scenes. *arXiv preprint arXiv:2410.13613*, 2024. 6, 8